BAYESIAN ADMITTANCE ESTIMATION AND MODEL SELECTION FOR FINITE-DIFFERENTIAL METHOD

Ziqi Chen

Submitted in Partial Fullfillment of the Requirements
for the Degree of

MASTER OF SCIENCE

Approved by:
Dr. Ning Xiang, Chair
Dr. Jonas braasch
Chris Perry

School of Architecture
Rensselaer Polytechnic Institute
Troy, New York

[August 2021]
Submitted July 2021

CONTENTS

LIST OF TABLES iii

LIST OF FIGURES iv

ACKNOWLEDGMENT v

ABSTRACT vi

1. INTRODUCTION 1

2. FINITE DIFFERENTIAL TIME DOMAIN METHOD 2

2.1 Stability 3

2.2 Numerical dispersion 4

2.3 Source 4

2.3.1 Source shape 5

2.4 Boundary condition 6

2.5 Auxiliary differential equation 8

3. BAYESIAN INFERENCE 14

3.1 Bayesian model selection 14

3.2 Bayesian parameter estimation 15

3.3 Unified framework 16

3.4 Nested sampling 16

3.4.1 Likelihood function 18

3.4.2 Prior assignment 18

3.4.3 Sampling results 19

4. VERIFICATION 22

5. SUMMARY 24

REFERENCES 25

LIST OF TABLES

3.1 Predicted parameters from Bayesian parameter estimation for a $\{Q = 1, S = 1\}$ broadband admittance model. 19

LIST OF FIGURES

2.1 One-dimensional first-order FDTD scheme around the n^{th} temporal step and i^{th} spatial step. 4

2.2 Impulse response in a tube (a) at the source node; (b) at the observation point. The tube is terminated by absorptive boundaries at both sides. The driving function is temporally Unit sample sequence and spatially Dirac delta function. 6

2.3 Impulse response in a tube (a) at the source node; (b) at the observation point. The tube is terminated by absorptive boundaries at both sides. The driving function is temporally Unit sample sequence and spatially Gaussian function. . 7

2.4 Impulse response in a tube (a) at the source node; (b) at the observation point. The tube is terminated by absorptive boundaries at both sides. The driving function is temporally Chebyshev Type 2 low-pass filter and spatially Dirac delta function. 7

2.5 Impulse response in a tube (a) at the source node; (b) at the observation point. The tube is terminated by absorptive boundaries at both sides. The driving function is temporally Chebyshev Type 2 low-pass filter and spatially Gaussian function. 8

3.1 Main steps of nested sampling for a single model. 17

3.2 Examples for surface admittance model sampling from the measured data with different orders of Q and S. Solid line is the measured surface admittance and dashed lines are admittance models associated with parameters obtained from Bayesian sampling. Q is the number of real-valued poles, and S is the number of complex-valued poles. 20

3.3 Bayes factors over the model set containing 5-13 parameters. $\mathbf{H}_{9a}$ denotes the model with $Q = 2, S = 1$, while $\mathbf{H}_{9b}$ denotes the model with $Q = 0, S = 2$. . . . 21

4.1 Surface admittance of the simulation results in comparison with the measurement data and the boradband admiitance model. 22

ACKNOWLEDGMENT

First, I would like to express my appreciation and gratefulness to my advisor, Dr. Ning Xiang. I cannot appreciate the precious advice and knowledge he shared with me during the thesis working more. His belief in his students' potential and his passion for acoustics inspire me a lot to do my best work. It is unforgettable for me that Dr. Xiang spent the time leading me the way. I also thank Dr. Jonas Braasch for his professionally teaching through the program. I would like to thank Dr. Tom Jasa for his help on explaining my confusion. I also want to thank Bill Bergman for his help on building the tubes. I am grateful for all my classmates in the program, and hope we can stay connected for years to come.

ABSTRACT

Surface acoustic impedance or admittance at the boundary is essential for estimating and evaluating a room's acoustic performance. In this article, a Bayesian-based model selection method and parameter estimation is presented to predict the admittance beyond the frequency limit of measurement. A frequency-dependent admittance model is chosen to estimate the boundary condition. The Bayesian-network sampling approach presented in this article shows the capability to predict the surface admittance boudary condition dependent on the frequency. This Bayesian method demonstrates a clear estimation of the pole number and parameters of the chosen frequency-dependent admittance model. The analysis results indicate the potential of applying the Bayesian-based method on boundary condition estimation.

CHAPTER 1
INTRODUCTION

In room acoustics, simulations play an important role in exploring sound propagation in an enclosed space, useful in many fields, like building and vehicle design. One popular kind of solution for room acoustics simulations is geometrical acoustics methods [1]. Geometrical acoustics methods simplify the sound propagation and reflection to make the computation more manageable [2]. Unfortunately, these simplifications undermine the accuracy of the simulation results since many factors that influence or even govern the sound motion are neglected. Another popular kind of solution to room acoustics simulations is wave-based methods, in which the governing wave equations are solved numerically. Unlike geometrical acoustics methods' requirement for absorption coefficients and reflectances to define the boundary conditions, wave-based methods require the surface impedance or admittance data to solve the governing equation of sound waves. Models were developed to describe arbitrary boundary conditions. Tam and Auriault [3] proposed a three-parameter broadband impedance model, while Fung and Ju [4] proposed a similar model on reflection coefficient. Reyman [5] modified the three-parameter impedance model to allow the application of recursive convolution. Li's model [6] combines the three-parameter model and some features of the multipole impedance model. An offset is introduced into the multipole broadband model by Dragana [7]. Zhao [8] converted the frequency-domain model to a Z-domain model.

Surface impedance boundary conditions are considered to be superior to absorption boundary conditions [1] because surface impedance contains more information about the boundary than the absorption coefficient, such as the phase changes after reflections. Bin [9] applied the second-order finite-differential scheme to the frequency response function impedance model. The second-order differential form was decreased by Troian and Dragna [10] into first-order differential form with auxiliary functions. Pind [2] applied the spectral element method to the time-domain auxiliary-differential impedance model.

CHAPTER 2
FINITE DIFFERENTIAL TIME DOMAIN METHOD

Finite-differential time-domain is a widely used simulation strategy in electromagnetism [11] and acoustics, since its simplicity for understanding and implementation. The FDTD method divides both temporal and spatial domain into small grids, and approximates the solution. Using volumetric meshes, The FDTD yields accurate results.

Yee [12] first proposed the finite-differential time-domain method for solving scattering problems of electromagnetic waves. Then the FDTD method was further developed in the field acoustics to solve the linearized Euler equations. The sound propagation in a lossless medium can be expressed by a pair of first-order differential equations:

$$\begin{aligned} \frac{\partial \boldsymbol{v}}{\partial t} &= -\frac{1}{\rho}\nabla \boldsymbol{p}, \\ \frac{\partial \boldsymbol{p}}{\partial t} &= -\rho\, \mathrm{c}^2 \nabla \cdot \boldsymbol{v}, \end{aligned} \tag{2.1}$$

where $\boldsymbol{v}_t$ and $\boldsymbol{p}_t$ represent the particle velocity and the sound pressure in the time domain, ρ is the density of the medium, c is the speed of sound in air, and ∇ and $\nabla\cdot$ are spatial gradient and divergence operations. With sufficiently small temporal difference and spatial difference, the sound pressure can be expressed in a discretized form as

$$p(x, y, z, t) \approx p(i \cdot \Delta x, j \cdot \Delta y, k \cdot \Delta z, n \cdot \Delta t) = p^{(n)}_{i,j,k}, \tag{2.2}$$

where $\Delta x, \Delta y$, and Δz are the spatial steps in x-, y-, and z- directions, Δt is the temporal step, $\{i, j, k\}$ and n represent the spatial and temporal index positions. In the same way, the discretized form of the sound pressure is

$$v_x(x, y, z, t) \approx p(i + 1/2 \cdot \Delta x, j \cdot \Delta y, k \cdot \Delta z, n + 1/2 \cdot \Delta t) = v^{(n+1/2)}_{i+1/2,j,k}. \tag{2.3}$$

$$v_y(x, y, z, t) \approx p(i \cdot \Delta x, j + 1/2 \cdot \Delta y, k \cdot \Delta z, n + 1/2 \cdot \Delta t) = v^{(n+1/2)}_{i,j+1/2,k}. \tag{2.4}$$

$$v_z(x, y, z, t) \approx p(i \cdot \Delta x, j \cdot \Delta y, k + 1/2 \cdot \Delta z, n + 1/2 \cdot \Delta t) = v^{(n+1/2)}_{i,j,k+1/2}. \tag{2.5}$$

Taking one-dimensional sound pressure and particle velocity as example, the both sides of

Equation (2.1) can be approximated by,

$$\frac{\partial \boldsymbol{v}}{\partial t} = \frac{v(x, t+\Delta t) - v(x,t)}{\Delta t}, \tag{2.6}$$

$$\nabla \boldsymbol{p} = \frac{\partial \boldsymbol{p}}{\partial x} = \frac{p(x+\Delta x, t) - p(x,t)}{\Delta x}. \tag{2.7}$$

Substitution of Equation (2.6) and (2.7) into Equation (2.1) leads to

$$\frac{v(x, t+\Delta t) - v(x,t)}{\Delta t} = -\frac{1}{\rho}\frac{p(x+\Delta x, t) - p(x,t)}{\Delta x}, \tag{2.8}$$

$$\frac{v_{i+1/2}^{(n+1/2)} - v_{i+1/2}^{(n-1/2)}}{\Delta t} = -\frac{1}{\rho}\frac{p_{i+1}^{(n)} - p_{i}^{(n)}}{\Delta x}. \tag{2.9}$$

Rearranging Equation (2.9) results in

$$v_{i+1/2}^{(n+1/2)} = v_{i+1/2}^{(n-1/2)} - \frac{\sigma}{\rho\,\mathrm{c}}\left[p_{i+1}^{(n)} - p_{i}^{(n)}\right], \tag{2.10}$$

with

$$\sigma = \mathrm{c}\,\frac{\Delta t}{\Delta x}, \tag{2.11}$$

where σ is Courant number, and ρc is the characteristic resistance of the medium [13]. In similar fashion, Equation (2.2) leads to another update equation

$$p_{i}^{(n+1)} = p_{i}^{(n)} - \rho\,\mathrm{c}\,\sigma\left[v_{i+1/2}^{(n+1/2)} - v_{i-1/2}^{(n+1/2)}\right]. \tag{2.12}$$

These two equations are called update equations of the first-order wave equations.

Figure 2.1 illustrates staggered grids for 1D finite-difference scheme around nth temporal step and ith spatial step.

2.1 Stability

To satisfy the stability and consistency requirement [14], the Courant number of the finite difference scheme should be chosen no more than its upper bound. Numerically, the value of the Courant number σ follows

$$\sigma \leqslant \sqrt{D}, \tag{2.13}$$

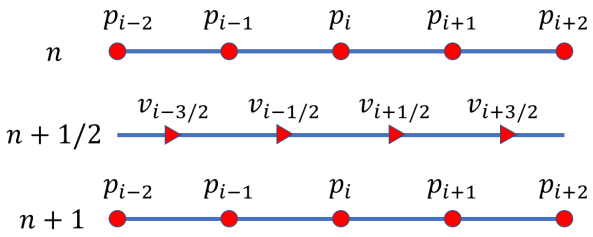

Figure 2.1: One-dimensional first-order FDTD scheme around the n^{th} temporal step and i^{th} spatial step.

where D is the number of spatial dimensions. For example, D is equal to 3 for three-dimensional simulations, and is 2 for two-dimensional simulations. The value of the Courant number affects the amound of numerical dispersion and the simulation duration [15]. Note that in one-dimensional simulation with σ chosen as unity, the FDTD yields no numerical errors.

2.2 Numerical dispersion

In reality, the velocity of the sound propagating in a non-dispersive medium is identical in all directions and independent of frequency. However, in a FDTD simulation, the phase velocities are dependent on both frequency and the direction of propagation [16]. The high-frequency components travels in lower speed, resulting in a visible 'tail' following the direct sound. This phenomenon or artifact is referred to as numerical dispersion, and is mainly caused by the inherent limitation of finite difference methods. To minimize this artifact, the Courant number should not exceed its upper stability bound, and simulations should employ an over 13 times temporal sampling [14].

2.3 Source

The source function is chosen carefully to minimize the numerical limitation of the FDTD method. For a hard source, the source node is equal to the value of the driving function. Since the source is independent of the incoming sound waves, it is a totally reflective boundary that is undesirable. Zhao [17] implemented a soft source which is the sum of the driving function and the update equation at the source node.

$$p^{(n+1)}(i_{\text{src}}) = \{p^{(n+1)}(i_{\text{src}})\} + S^{(n+1)}(i_{\text{src}}). \tag{2.14}$$

where $p^{(n+1)}(i_{\mathrm{src}})$ is the sound pressure at the nth time step at the source node, $\{p^{(n+1)}(i_{\mathrm{src}})\}$ is the result of the update equation at the source node, and $S^{(n)}(i_{\mathrm{src}})$ is the driving function.The soft source allows the incoming sound wave to pass through it instead of being reflected. However, the shape of the impulse response implemented this way is not similar to the driving function [15] because of the 'echo' of the previous source term. To cancel the 'echo,' Schneider [15] implemented a transparent source as the summation of the driving function, the update equation, and the convolution of the driving function and the impulse response at the source node. Schneider's method requires the impulse responses at source nodes which are measured before the actual simulation. The convolution of the grid's response and the driving function is compensated for during the simulation. A transparent source can be numerically expressed by

$$p^{(n+1)}(i_{\mathrm{src}}) = \{p^{(n+1)}(i_{\mathrm{src}})\} + S^{(n+1)}(i_{\mathrm{src}}) - \sum_{m=0}^{n} h^{(n-m+1)} S^{(n)}(i_{\mathrm{src}}), \tag{2.15}$$

where $h^{(n)}$ is the pre-measured impulse response at the source node. The transparent source radiates a sound field resembling that radiated by a hard source without the scattering of the source node. Although in real world, it is impossible to treat a loudspeaker as a transparent source, implementation of the transparent source is helpful for better understanding the sound propagation.

2.3.1 Source shape

One major inherent limitation of the FDTD method is numerical dispersion. The numerical dispersion contributes to the phase velocity difference, which is dependent on the frequency. This difference in the phase velocity leads to the accumulation of the numerical error, which results in a 'tail' following the direct sound. Due to the accumulation of numerical errors, the driving function of the domain cannot simply set as a Unit sample sequence, otherwise the numerical dispersion yields unreliable impulse response (see Figure 2.2). Two widely employed driving function are Gaussian pulse and Black-Harris window [18]. If the bandwidth is too wide, the Gaussian pulse will introduce spectral ripples [16](see Figure 2.3). Another popular choice for the excitation signal is Ricker wavelet, which is a second derivative of a Gaussian function.

To minimize the numerical dispersion or to delay the showing-up of the 'tail' as late

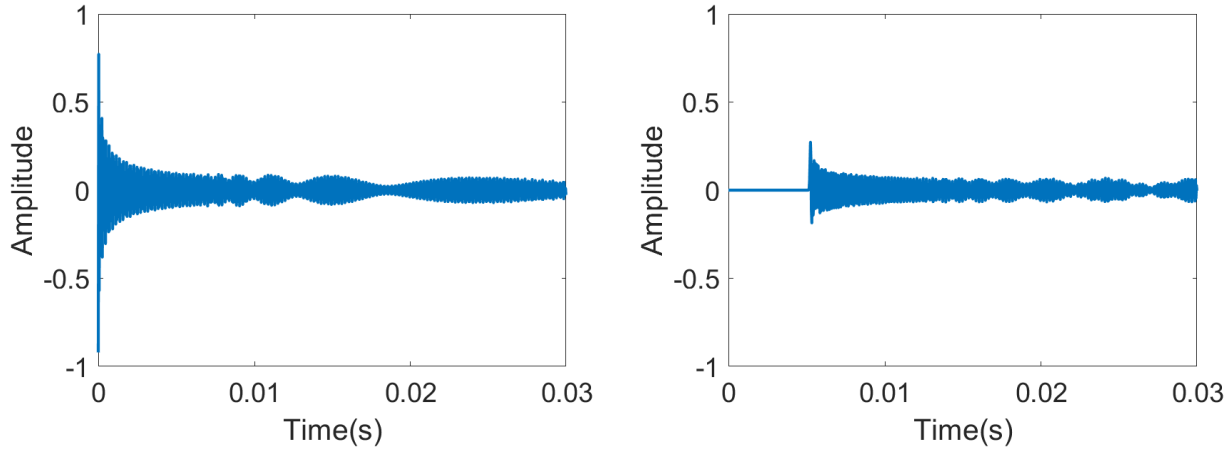

(a) **(b)**

Figure 2.2: Impulse response in a tube (a) at the source node; (b) at the observation point. The tube is terminated by absorptive boundaries at both sides. The driving function is temporally Unit sample sequence and spatially Dirac delta function.

as possible, a low-pass IIR filter is applied to the driving function. However, if the spatial domain is excited by one single source node, which is unity in spatial frequency domain, noise and numerical errors will be introduced (see Figure 2.4). To smooth the impulse response, we drive multiple nodes with the same temporal waveform but scale each by different amounts, and the scale factors are determined by a Gaussian impulse. Figure 2.4 demonstrates that with the tube driven both temporally and spatially, the impulse response suffers less from the phase error. Note that this method amplifies the impulse response as well.

2.4 Boundary condition

Modeling the sound wave propagation in an enclosure requires assignment of boundary conditions. In this work, two types of boundary models are investigated to solve the underlying wave equation. The first type is absorptive boundaries. Absorptive boundaries are used to terminate the simulation at the edge of the domain, avoiding the sound waves reflected into the grids again. One straightforward way to do this is to set the impedance of boundary exactly equivalent to the characteristic impedance of air. However, due to inherent limitation of the FDTD, the accumulated small numerical errors will lead to incomplete absorption of the terminations. One popular method to solve this problem is Mur's absorbing boundary

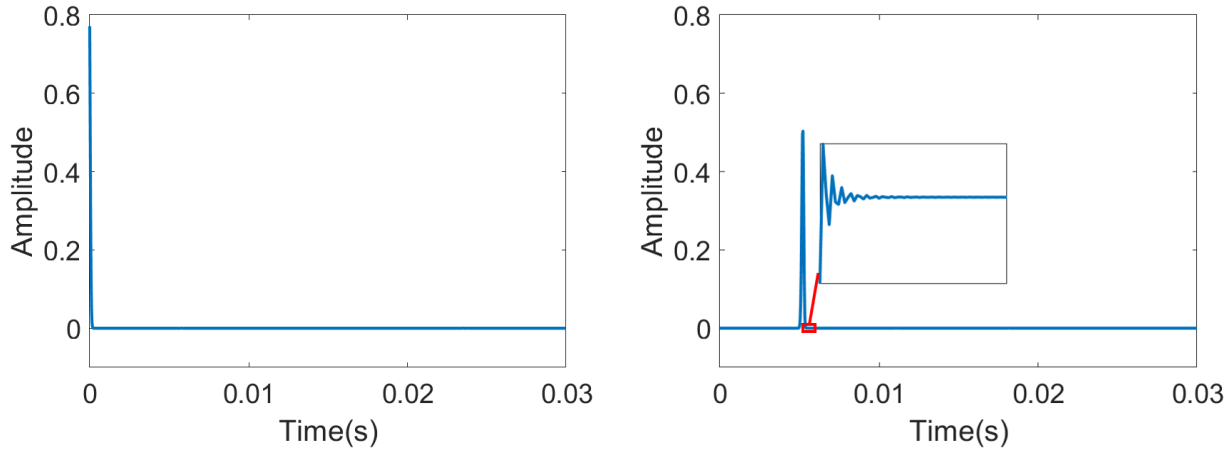

(a) (b)

Figure 2.3: Impulse response in a tube (a) at the source node; (b) at the observation point. The tube is terminated by absorptive boundaries at both sides. The driving function is temporally Unit sample sequence and spatially Gaussian function.

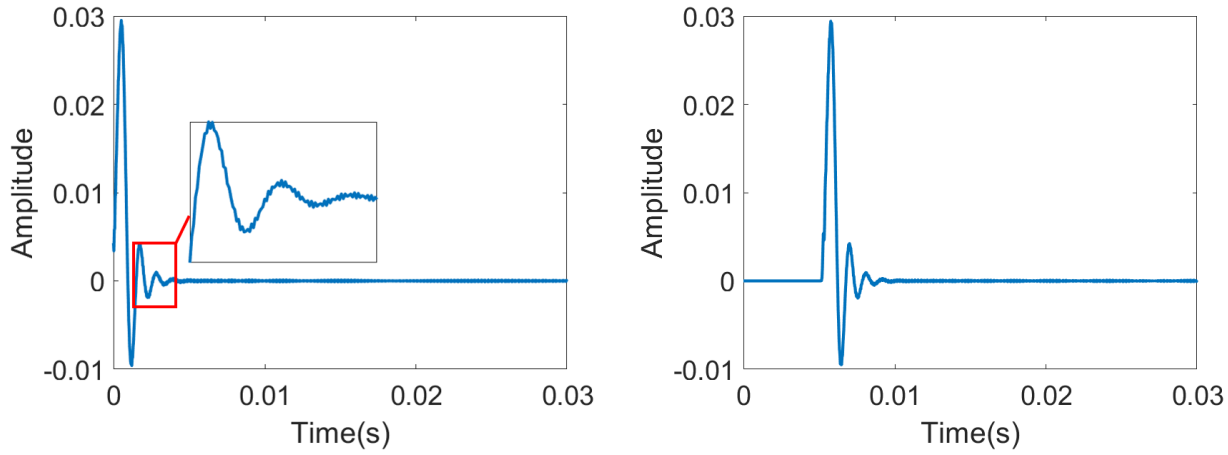

(a) (b)

Figure 2.4: Impulse response in a tube (a) at the source node; (b) at the observation point. The tube is terminated by absorptive boundaries at both sides. The driving function is temporally Chebyshev Type 2 low-pass filter and spatially Dirac delta function.

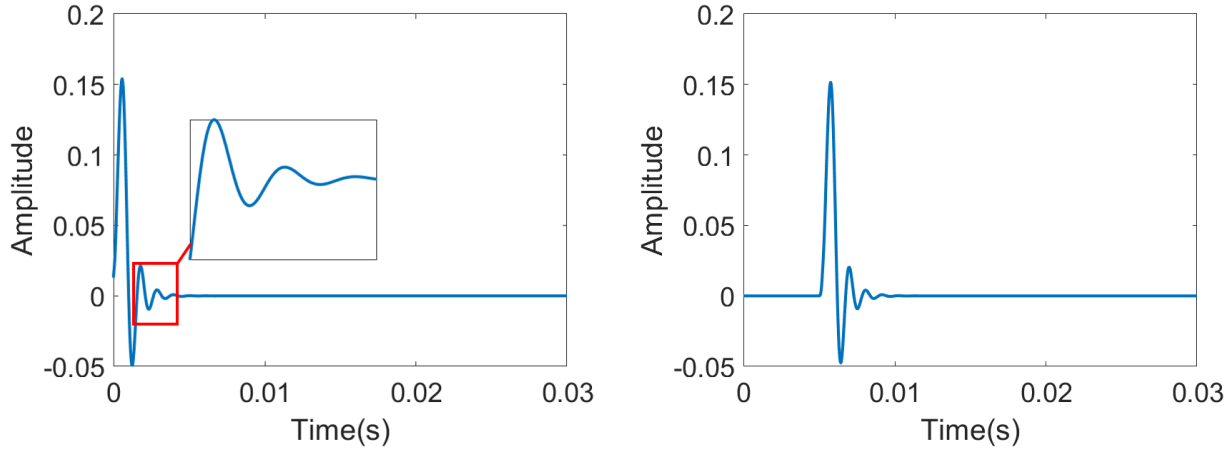

(a) **(b)**

Figure 2.5: Impulse response in a tube (a) at the source node; (b) at the observation point. The tube is terminated by absorptive boundaries at both sides. The driving function is temporally Chebyshev Type 2 low-pass filter and spatially Gaussian function.

condition. For example, in one dimension, the sound pressure at absorbing boundary is

$$p_0^{(n+1)} = p_1^{(n)} + \frac{\sigma - 1}{\sigma + 1}\left[p_1^{(n+1)} - p_0^{(n)}\right]. \tag{2.16}$$

Mur's absorbing boundary condition is valid for normal incidence, but it is known to be erroneous for oblique incidences [19].

2.5 Auxiliary differential equation

The complex-valued surface impedance in the frequency domain, $\underline{Z}_s(\omega)$, is determined by

$$\underline{Z}_s(\omega) = \frac{\underline{P}(\omega)}{\underline{V}(\omega)}, \tag{2.17}$$

where $\underline{P}(\omega)$ and $\underline{V}(\omega)$ are the sound pressure and the particle velocity normal to the surface in frequency domain. So the surface admittance $\underline{G}(\omega)$ is written as

$$\underline{G}(\omega) = \frac{1}{\underline{Z}_s(\omega)} = \frac{\underline{V}(\omega)}{\underline{P}(\omega)}. \tag{2.18}$$

Bin and Hussaini [9] developed a finite differential form for a multipole impedance model. Dragna [7, 10] expanded the multipole model to include the constant term Z_∞ and decom-

posed the second-order differential system to calculate the accumulators. In General, the admittance boundary conditions for the multipole model can be expressed as [7, 10, 2][1]

$$\begin{aligned}\underline{G}(\omega) = G_\infty + \sum_{q=1}^{Q} \frac{A_q}{\lambda_q + \mathrm{j}\omega} \\ + \sum_{s=1}^{S} \left(\frac{\underline{\Theta}_s}{\underline{\theta}_s + \mathrm{j}\omega} + \frac{\underline{\Theta}_s^*}{\underline{\theta}_s^* + \mathrm{j}\omega} \right),\end{aligned} \tag{2.19}$$

with

$$\underline{\Theta}_s = B_s + \mathrm{j}C_s, \tag{2.20}$$

$$\underline{\theta}_s = \alpha_s + \mathrm{j}\beta_s, \tag{2.21}$$

where Q is the number of real-valued poles, λ_q, S is the number of complex-values pole pairs, $[\theta_s, \theta_s^*]$, and G_∞, A_q, B_s, and C_s are real-valued coefficients. To ensure the system is causal and real, $\lambda_q, \alpha_s \in \mathbb{R}^+$. So Equation (2.19) can be written as[2]

$$\begin{aligned}\underline{G}(\omega) = G_\infty + \sum_{q=1}^{Q} \frac{A_q}{\lambda_q + \mathrm{j}\omega} \\ + \sum_{s=1}^{S} \left(\frac{B_s + \mathrm{j}C_s}{\alpha_s + \mathrm{j}\beta_s + \mathrm{j}\omega} + \frac{B_s - \mathrm{j}C_s}{\alpha_s - \mathrm{j}\beta_s + \mathrm{j}\omega} \right),\end{aligned} \tag{2.22}$$

leading to the particle velocity in frequency domain

$$\begin{aligned}V(\omega) = G_\infty P(\omega) + \sum_{q=1}^{Q} A_q \phi_q(\omega) \\ + \sum_{s=1}^{S} 2[B_s \psi_s^{(1)}(\omega) + C_s \psi_s^{(2)}(\omega)].\end{aligned} \tag{2.23}$$

[1]The equation here is slightly different from the Equation in Dragna's work because of different conventions used in Fourier Transform.

[2]Same as above

where ϕ_s , $\psi_s^{(1)}$, and $\psi_s^{(2)}$ are so-called accumulators, which are

$$(\mathrm{j}\omega + \lambda_q)\phi_q(\omega) = P(\omega), \tag{2.24a}$$
$$(\mathrm{j}\omega + \alpha_s)\psi_s^{(1)}(\omega) + \beta_s\psi_s^{(2)}(\omega) = P(\omega), \tag{2.24b}$$
$$(\mathrm{j}\omega + \alpha_s)\psi_s^{(2)}(\omega) - \beta_s\psi_s^{(1)}(\omega) = 0. \tag{2.24c}$$

Applying Inverse Fourier transform to Equation (2.23),

$$\begin{aligned} v_n(t) = G_\infty p(t) &+ \sum_{q=1}^{Q} A_q\phi_q(t) \\ &+ \sum_{s=1}^{S} 2[B_s\psi_s^{(1)}(t) + C_s\psi_s^{(2)}(t)], \end{aligned} \tag{2.25}$$

where ϕ_s , $\psi_s^{(1)}$, and $\psi_s^{(2)}$ in time domain are determined by differential equations

$$\begin{aligned} &\frac{\partial\phi_q}{\partial t} + \lambda_q\phi_q(t) = p(t), \\ &\frac{\partial\psi_s^{(1)}}{\partial t} + \alpha_s\psi_s^{(1)}(t) + \beta_s\psi_s^{(2)}(t) = p(t), \\ &\frac{\partial\psi_s^{(2)}}{\partial t} + \alpha_s\psi_s^{(2)}(t) - \beta_s\psi_s^{(1)}(t) = 0. \end{aligned} \tag{2.26}$$

With the accumulators sampled at half-integer time step $n + 1/2$ and the sound pressure p sampled at integer time step n, discretization of the accumulators and the sound pressure in

Equation (2.26) leads to

$$\frac{\phi_q(n+\frac{1}{2})-\phi_q(n-\frac{1}{2})}{\Delta t}+\lambda_q\frac{\phi_q(n+\frac{1}{2})+\phi_q(n-\frac{1}{2})}{2}=\frac{p^{(n+1)}+p^{(n)}}{2}, \tag{2.27}$$

$$\begin{aligned}\frac{\psi_s^{(1)}(n+\frac{1}{2})-\psi_s^{(1)}(n-\frac{1}{2})}{\Delta t}+\alpha_s\frac{\psi_s^{(1)}(n+\frac{1}{2})+\psi_s^{(1)}(n-\frac{1}{2})}{2}\\ +\beta_s\frac{\psi_s^{(2)}(n+\frac{1}{2})+\psi_s^{(2)}(n-\frac{1}{2})}{2}=\frac{p^{(n+1)}+p^{(n)}}{2},\end{aligned} \tag{2.28}$$

$$\begin{aligned}\frac{\psi_s^{(2)}(n+\frac{1}{2})-\psi_s^{(2)}(n-\frac{1}{2})}{\Delta t}+\alpha_s\frac{\psi_s^{(2)}(n+\frac{1}{2})+\psi_s^{(2)}(n-\frac{1}{2})}{2}\\ -\beta_s\frac{\psi_s^{(1)}(n+\frac{1}{2})+\psi_s^{(1)}(n-\frac{1}{2})}{2}=0,\end{aligned} \tag{2.29}$$

where Δt is the temporal step. Rearrangement of Equations (2.27)-(2.29) leads to the update equations

$$\phi_q(n+\frac{1}{2})=\frac{2-\lambda_q\Delta t}{2+\lambda_q\Delta t}\phi_q(n-\frac{1}{2})+\frac{2\Delta t}{2+\lambda_q\Delta t}\frac{p^{(n+1)}+p^{(n)}}{2}, \tag{2.30}$$

$$\begin{aligned}\psi_s^{(1)}(n+\frac{1}{2})=\frac{2-\alpha_s\Delta t}{2+\alpha_s\Delta t}\psi_s^{(1)}(n-\frac{1}{2})-\frac{\beta_s\Delta t}{2+\alpha_s\Delta t}\psi_s^{(2)}(n+\frac{1}{2})\\ -\frac{\beta_s\Delta t}{2+\alpha_s\Delta t}\psi_s^{(2)}(n-\frac{1}{2})\\ +\frac{2\Delta t}{2+\alpha_s\Delta t}\frac{p^{(n+1)}+p^{(n)}}{2},\end{aligned} \tag{2.31}$$

$$\begin{aligned}\psi_s^{(2)}(n+\frac{1}{2})=\frac{2-\alpha_s\Delta t}{2+\alpha_s\Delta t}\psi_s^{(2)}(n-\frac{1}{2})+\frac{\beta_s\Delta t}{2+\alpha_s\Delta t}\psi_s^{(1)}(n+\frac{1}{2})\\ +\frac{\beta_s\Delta t}{2+\alpha_s\Delta t}\psi_s^{(1)}(n-\frac{1}{2}).\end{aligned} \tag{2.32}$$

Substitution of Equation (2.31) into (2.32) with a few rearrangements leads to

$$\psi_s^{(1)}(n+\frac{1}{2}) = \frac{4K_1 - K_1^2 - K_2^2}{K_1^2 + K_2^2}\psi_s^{(1)}(n-\frac{1}{2}) - \frac{4K_2}{K_1^2 + K_2^2}\psi_s^{(2)}(n-\frac{1}{2}) + \frac{2\Delta t K_1}{K_1^2 + K_2^2}\frac{p^{(n+1)} + p^{(n)}}{2}, \tag{2.33}$$

where

$$K_1 = 2 + \alpha_s \Delta t; \qquad K_2 = \beta_s \Delta t. \tag{2.34}$$

Similarly, inserting Equation (2.33) into (2.32) leads to solving Equation (2.32)

$$\psi_s^{(2)}(n+\frac{1}{2}) = \frac{4K_1 - K_1^2 - K_2^2}{K_1^2 + K_2^2}\psi_s^{(2)}(n-\frac{1}{2}) + \frac{4K_2}{K_1^2 + K_2^2}\psi_s^{(1)}(n-\frac{1}{2}) + \frac{2\Delta t K_2}{K_1^2 + K_2^2}\frac{p^{(n+1)} + p^{(n)}}{2}. \tag{2.35}$$

Then discrestization of Equation (2.25) leads to its finite-difference formulation

$$v^{(n+1/2)} = G_\infty \frac{p^{(n+1)} + p^{(n)}}{2} + \sum_{q=1}^{Q} A_q \phi_q(n+\frac{1}{2}) + \sum_{s=1}^{S} 2[B_s \psi_s^{(1)}(n+\frac{1}{2}) + C_s \psi_s^{(2)}(n+\frac{1}{2})], \tag{2.36}$$

Application of Equation (2.36) results in the update boundary equation for the sound pressure $p^{(n+1)}$ at the boundary

$$\begin{aligned} p^{(n+1)} = -p^{(n)} + \Psi \cdot \Bigg\{ & v^{(n+\frac{1}{2})} - \sum_{q=1}^{Q} A_q \cdot \frac{2 - \lambda_q \Delta t}{2 + \lambda_q \Delta t}\phi_q(n-\frac{1}{2}) \\ & - \sum_{s=1}^{S} 2B_s \left[\frac{4K_1 - K_1^2 - K_2^2}{K_1^2 + K_2^2}\psi_s^{(1)}(n-\frac{1}{2}) \right. \\ & \left. - \frac{4K_2}{K_1^2 + K_2^2}\psi_s^{(2)}(n-\frac{1}{2}) \right] \\ & - \sum_{s=1}^{S} 2C_s \left[\frac{4K_1 - K_1^2 - K_2^2}{K_1^2 + K_2^2}\psi_s^{(2)}(n-\frac{1}{2}) \right. \\ & \left. + \frac{4K_2}{K_1^2 + K_2^2}\psi_s^{(1)}(n-\frac{1}{2}) \right] \Bigg\}, \end{aligned} \tag{2.37}$$

where

$$\Psi = \left[\frac{G_\infty}{2} + \sum_{q=1}^{Q} \frac{A_q \Delta t}{2 + \lambda_q \Delta t} + \sum_{s=1}^{S} 2 \left(\frac{B_s \Delta t K_1}{K_1^2 + K_2^2} + \frac{C_s \Delta t K_2}{K_1^2 + K_2^2} \right) \right]^{-1} \tag{2.38}$$

Therefore, the ADE-FDTD algorithm for modeling the arbitrary boundary represents a three-step fully explicit procedure. To be precise, at nth time step, the $p(n), v(n-\frac{1}{2}), \phi_q(n-\frac{1}{2}), \psi_s^{(1)}(n-\frac{1}{2})$, and $\psi_s^{(2)}(n-\frac{1}{2})$ are available. First, the $v(n+\frac{1}{2})$ component is calculated through Yee's algorithm update equation [Equation (2.10)]. And then $p^{(n+1)}$ is calculated using Equation (2.37). Finally, $\phi_q(n+\frac{1}{2}), \psi_s^{(1)}(n+\frac{1}{2})$, and $\psi_s^{(2)}(n+\frac{1}{2})$ are calculated using Equation (2.30), (2.33) and (2.35) with a set of $v(n+\frac{1}{2})$, and then repeat another cycle for next step.

CHAPTER 3
BAYESIAN INFERENCE

The Admittance model in Equation (2.19) formulated by Dragna [7] is now applied to the measurement data. Two-levels of inference are required to verify and validate the ADE-FDTD. Firstly, the numbers of the real-valued poles and the conjugate pole pairs remain unknown. And then, after obtaining the proper numbers of poles, the values of the coefficients need determining.

There are a set of finite competing models potential describing the experiment data. Define the model set as $\{\mathbf{H}_{00}, \mathbf{H}_{01}, ..., \mathbf{H}_{QS}\}$. Each model, $\mathbf{H}_{qs}$, is associated with q number of real poles and s number of conjugate pole pairs, with $q \in [0, Q]$ and $s \in [0, S]$. As shown in Equation (2.22), each step increase in q leads to 2 more parameters in the model, and 4 more parameters for each unity increase in s. Bayesian inference applied to the parameter estimation is known as the first level of inference, while the model selection is the second level of inference, also referred to as a higher level of inference [20]. As one should determine which model among the competing models set is preferred to predict the data before estimating the parameters in the model, the top-down approach is logical [21]. Therefore, the discussion begins with the model selection, followed by the parameter estimation.

3.1 Bayesian model selection

In some cases, if the complexity of a model is too high, it tends to fit everything in the known data perfectly but fails to fit the unknown data, which is known as overfit. To avoid the overfitting phenomenon, the model selection applies Bayes' theorem to determine the probability of an arbitrary model $\mathbf{H}_{qs}$ among a finite set of models $\{\mathbf{H}_{00}, \mathbf{H}_{01}, ..., \mathbf{H}_{QS}\}$, given the data, $\mathbf{D}$, and the background information, I. Bayesian theorem can be written as

$$p(\mathbf{H}_{qs}|\mathbf{D}, I) = \frac{p(\mathbf{D}|\mathbf{H}_{qs}, I)p(\mathbf{H}_{qs}|I)}{p(\mathbf{D}|I)}. \tag{3.1}$$

where $p(\mathbf{H}_{qs}|\mathbf{D}, I)$ is the posterior probability of the model, $p(\mathbf{D}|\mathbf{H}_{qs}, I)$ is the likelihood of the model given the measured data, $p(\mathbf{H}_{qs}|I)$ is the prior probability of the model, and $p(\mathbf{D}|I)$ is the probability of observing the experimental data. $p(\mathbf{D}|\mathbf{H}_{qs}, I)$ is also referred

to as 'Bayesian evidence' [22], which is the key index for evaluating the models. Equation (3.1) indicates that in the presence of data, how the prior knowledge about the model is updated [21].

Pursuing Bayesian model evaluation leads to the employment of Bayes factor, also known as odds ratio [23], for making comparison between two competing models [21],

$$B_{ij} = \frac{p(\mathbf{H}_i|\mathbf{D}, I)}{p(\mathbf{H}_j|\mathbf{D}, I)} = \frac{p(\mathbf{D}|\mathbf{H}_i, I)}{p(\mathbf{D}|\mathbf{H}_j, I)}, \; i \neq j, \tag{3.2}$$

where i and j represent the numbers of the parameters that need estimation in total in the models. As discussed in Chapter 2, every unity increase in q leads to 2 more parameters in the model, and 4 more parameters for every unity increase in s. In this case, different models may have same number of parameters with different q and s. To distinguish one from another, $\mathbf{H}_{ia}$ denotes the model having i parameters with a lower s, while $\mathbf{H}_{ib}$ denotes the model having i parameters with a higher s. For example, the model with $q = 2, s = 1$ is referred to as $\mathbf{H}_{9a}$, while $\mathbf{H}_{9b}$ denotes the model with $q = 0, s = 2$.

For computational convenience, taking the logarithmic scale of both sides in Equation (3.2) leads to

$$L_{ij} = 10\log_{10}(B_{ij}) = 10\log_{10}(p(\mathbf{D}|\mathbf{H}_i, I)) - 10\log_{10}(p(\mathbf{D}|\mathbf{H}_j, I)). \tag{3.3}$$

In this way, the evidences for two competing models can be compared with each other quantitatively [20]. The higher the Bayes factor indicates that the model $\mathbf{H}_i$ i more preferred by the data than the model $\mathbf{H}_j$.

3.2 Bayesian parameter estimation

Once the model is selected based on the Bayes factor, the parameter needs estimating on the first level of inference. The broad admittance model contains a specific of parameters, including the offset, the poles and their coefficients. The parameter estimation applying Bayesian Theorem yields,

$$p(\boldsymbol{\theta}|\mathbf{H}, \mathbf{D}, I) = \frac{p(\mathbf{D}|\boldsymbol{\theta}, \mathbf{H}, I)p(\boldsymbol{\theta}|\mathbf{H}, I)}{p(\mathbf{D}|\mathbf{H}, I)}, \tag{3.4}$$

where I denotes the background information including a specific model is selected, $\mathbf{H}$ denotes the selected model, $\boldsymbol{\theta}$ denotes the set of parameters, $\{G_\infty; A; B; C; \lambda; \alpha; \beta\}$, in Equation (2.22), and $\mathbf{D}$ denotes the experimental data. Equation (3.4) demonstrates how the prior knowledge of the parameter, $p(\boldsymbol{\theta}|\mathbf{H}, I)$, is updated through the likelihood, $p(\mathbf{D}|\boldsymbol{\theta}, \mathbf{H}, I)$.

3.3 Unified framework

The rearrangement of Equation (3.4) leads to

$$p(\boldsymbol{\theta}|\mathbf{H}, \mathbf{D}, I) \cdot p(\mathbf{D}|\mathbf{H}, I) = p(\mathbf{D}|\boldsymbol{\theta}, \mathbf{H}, I) \cdot p(\boldsymbol{\theta}|\mathbf{H}, I) \tag{3.5}$$

Since the integral of any probability density over the entire parameter space is equal to unity, integrating both sides of Equation (3.5) results in

$$p(\mathbf{D}|\mathbf{H}, I) = \int_{\boldsymbol{\theta}} p(\mathbf{D}|\boldsymbol{\theta}, \mathbf{H}, I) \cdot p(\boldsymbol{\theta}|\mathbf{H}, I) \mathrm{d}\boldsymbol{\theta} \tag{3.6}$$

Equation (3.6) indicates that the evidence of a specific model is determined by integrating the product of the likelihood and the prior over the whole parameter space [21]. According to Equation (3.5), both Bayesian model selection and parameter estimation can be unified into one framework. In this framework, the prior and the likelihood are inputs, while the evidence and the posterior are the output quantities.

3.4 Nested sampling

There are different sampling methods developed to calculate the Bayesian evidence that the Bayesian model selection and parameter estimation require. Laplace approximation approximates the probability density function with a Gaussian [22]. Importance sampling enables one to estimate the properties of a specific distribution with samples from a different distribution [22]. Nested sampling, first proposed by Skilling in 2004 [24], computing the evidence relying on random integration. This work relies on nested sampling to calculate the evidence of the posterior probability.

Figure 3.1 presents the general main steps for nested sampling. Firstly, an initial population is generated with all parameters generated randomly according to the uniform distributions. In our work, the size of the initial population is 500. Then, calculate the

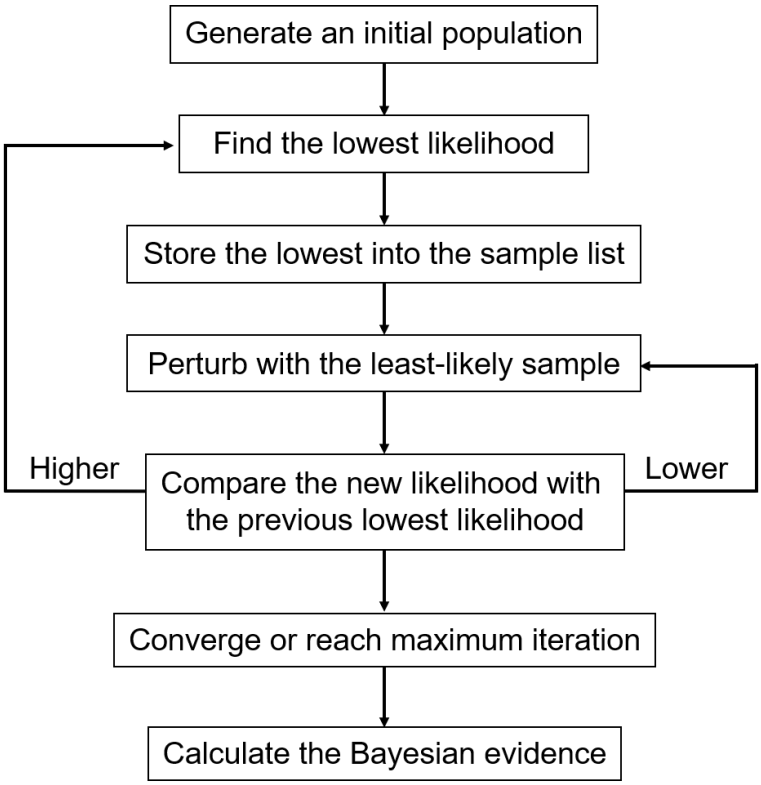

Figure 3.1: Main steps of nested sampling for a single model.

likelihood value of each sample, and find the minimum of the likelihood within the population. After identifying the minimum likelihood, push it into a sample list independent of the initial population and then perturb the parameters related to the least-likely sample randomly. The perturbing process includes generating a random number of random parameters and recalculating the likelihood value with the set of perturbed parameters. Repeat perturbing until finding a new sample with a higher likelihood value. Once the new likelihood value is higher than the lowest likelihood value pushed into the sample list in the last step, replace the parameters in the population associated with the least likely sample with these new values. After the initial population is updated, find the new lowest likelihood value within the population and then repeat the steps of recording and perturbing until the likelihoods of the sample population converge or until reaching the maximum number of iterations. In this way, the sample list recording the likelihood values is already sorted, and the summation of the list approximates the evidence of the model.

3.4.1 Likelihood function

The likelihood function is assigned as a student's t-distribution,

$$\mathcal{L}(\boldsymbol{\theta}) = \frac{\Gamma(K/2)}{2}\left(\pi\sum_{k=1}^{K}\varepsilon_k^2\right)^{-K/2}, \tag{3.7}$$

where K is the total number of measured data points, $\Gamma(\cdot)$ is the Gamma function, ε_k^2 is the squared error between measured and modeled surface admittance data, determined by

$$\varepsilon_k^2 = \mathrm{Re}[G_{\mathrm{measure}}(f_k) - G_{\mathrm{model}}(f_k)]^2 + \mathrm{Im}[G_{\mathrm{measure}}(f_k) - G_{\mathrm{model}}(f_k)]^2, \tag{3.8}$$

where G_{measure} is the measured data, G_{model} is the modeled data derived from Equation (2.22), and f_k is the frequency point where the surface admittance data was measured.

3.4.2 Prior assignment

Before involving any data, the prior knowledge about the broadband admittance model in Equation (2.22) is very limited. The only available background knowledge is that for any realistic physical system, it must be causal and real. As stated in Section 2, λ_q and α_s must be real positive values to meet the casualty requirement. To make sure the parameter space is fully explored, the parameter ranges should be wide. The principle of maximum entropy yields a uniform probability density function with wide parameters range for each parameter. The prior probability density for each parameter is defined as

- $p(G_\infty)$ = Uniform (-1,1)
- $p(A_q)$ = Uniform $(-2\times10^5, 2\times10^5)$
- $p(\lambda_q)$ = Uniform $(0, 2\times10^5)$
- $p(B_s)$ = Uniform $(-2\times10^5, 2\times10^5)$
- $p(C_s)$ = Uniform $(-2\times10^5, 2\times10^5)$
- $p(\alpha_s)$ = Uniform $(0, 2\times10^5)$
- $p(\beta_s)$ = Uniform $(-2\times10^5, 2\times10^5)$

Table 3.1: Predicted parameters from Bayesian parameter estimation for a $\{Q = 1, S = 1\}$ broadband admittance model.

Coefficients	Values	Deviations
G_∞	0.5371	0.0133
A_1	-3.4716e+04	1.6687e+03
B_1	2.0165e+03	3.7265
C_1	2.721e+02	3.4323
λ_1	6.4763e+04	1.6036e+03
α_1	1.5301e+03	2.4324
β_1	-1.0057e+04	2.6238

3.4.3 Sampling results

Figure 3.2 presents some examples from the Bayesian inferences. With $Q = 0$, the broadband admittance model is the same as the conventional multipole admittance model. When $Q = 0, S = 1$, the model already fits the measurement data well. As shown in the figure, the matching is getting better With the number of poles getting higher. However, more computational efforts are required by the more complicated models as well, since the increase in Q and S leads to more parameters in the estimation. Undesirable inaccuracy and overfitting may occur when the model gets too complicated. Figure 3.3 illustrates the Bayes factors calculated from the evidence of the Bayesian inference for the models with different numbers of parameters. Note that because the model with $S = 0$ doesn't fit the measurement data, they are ruled out of the comparison. Given the data in this example, the Bayes factor $L_{6,4}$ is the highest, suggesting that the model with $Q = 1, S = 1$ is most preferred by the data over the model with $Q = 0, S = 1$. This selection indicates that one real-valued pole and one pair of conjugate poles are sufficient for Bayesian inference to produce the desired surface admittance.

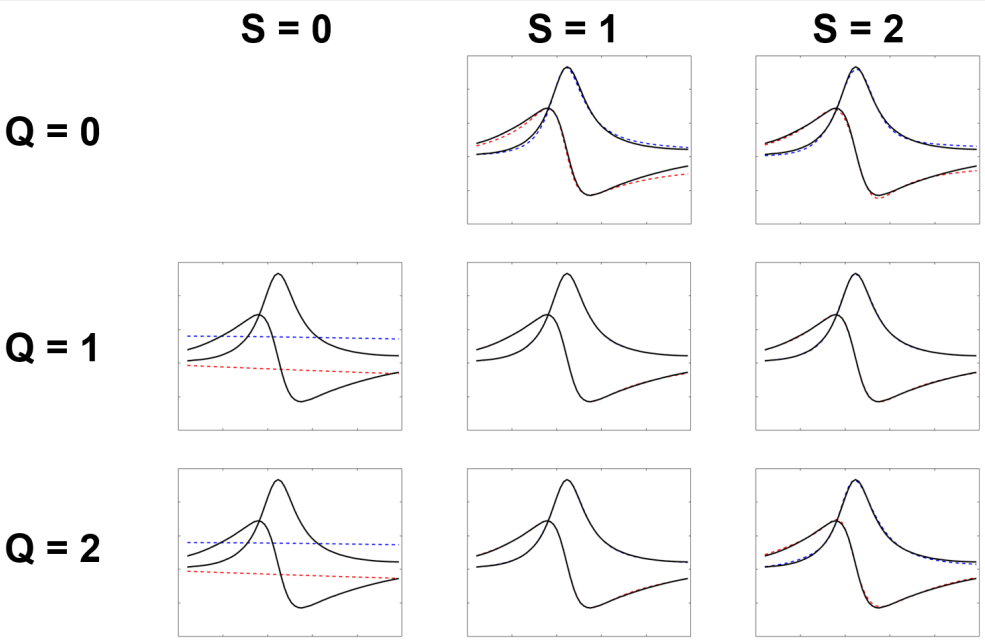

Figure 3.2: Examples for surface admittance model sampling from the measured data with different orders of Q and S. Solid line is the measured surface admittance and dashed lines are admittance models associated with parameters obtained from Bayesian sampling. Q is the number of real-valued poles, and S is the number of complex-valued poles.

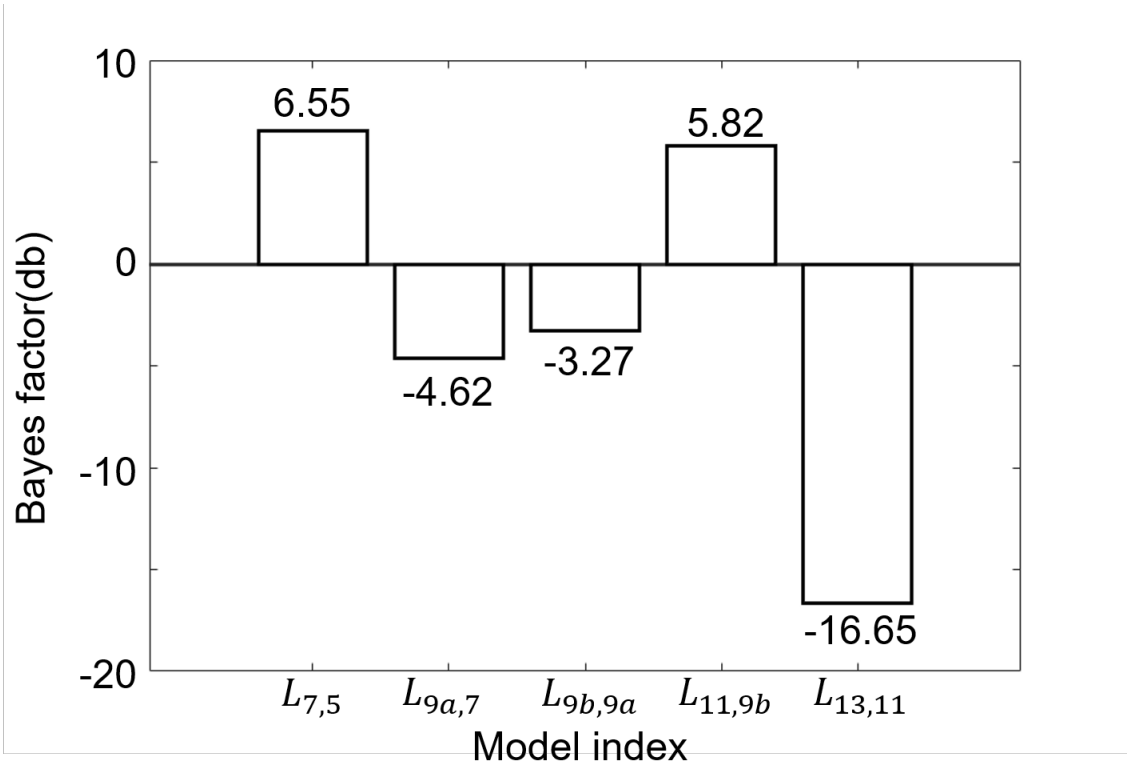

Figure 3.3: Bayes factors over the model set containing 5-13 parameters. $\mathbf{H}_{9a}$ denotes the model with $Q = 2, S = 1$, while $\mathbf{H}_{9b}$ denotes the model with $Q = 0, S = 2$.

CHAPTER 4
VERIFICATION

With the ADE-FDTD formulated in Section 2, one can simulate the sound wave propagation in the tube. To be specified, the tube used in the simulation is terminated with Mur's ABC(absorbing boundary condition) on the left side, and the right side of the tube is terminated with an arbitrary boundary whose parameters are estimated against the measurement data. The tube dimension is 0.05 meter $\times$ 0.05 meter $\times$ 10 meter, and the sound source is a plane parallel to yz-plane placed at the middle (5 meter) of the tube.

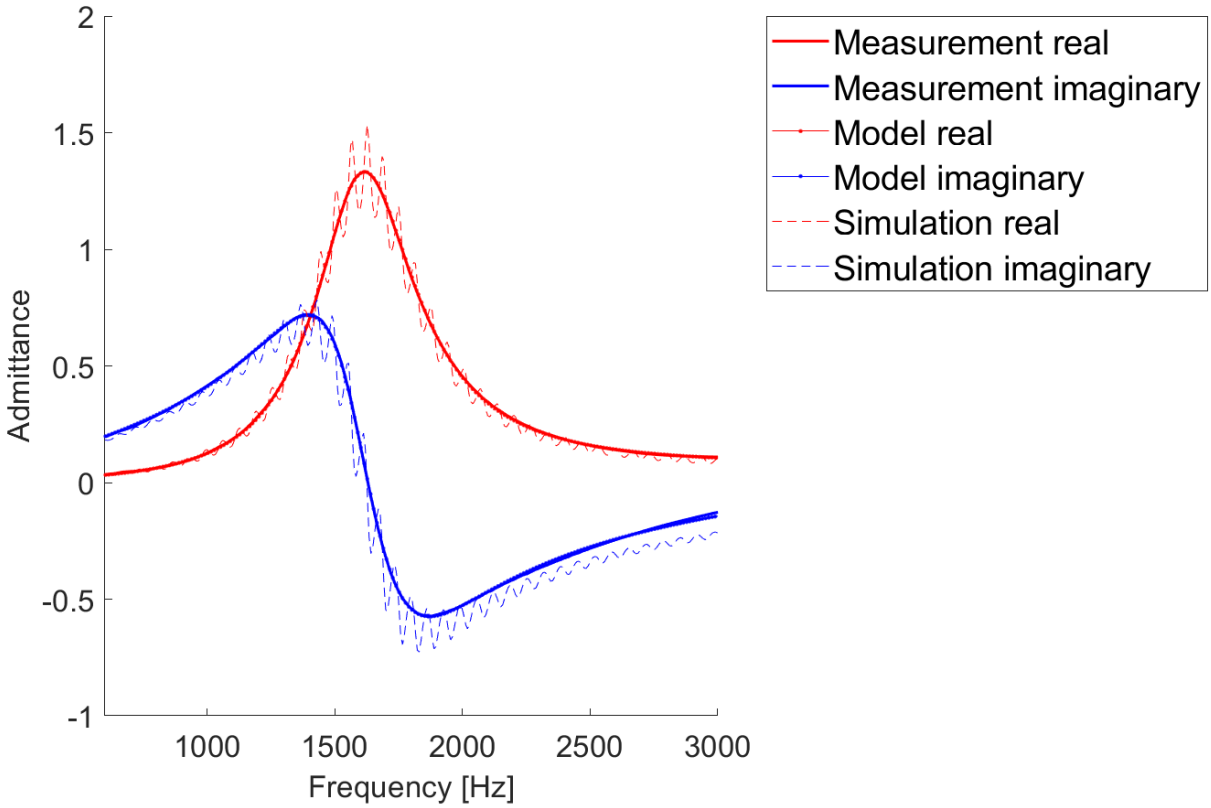

Figure 4.1: Surface admittance of the simulation results in comparison with the measurement data and the boradband admiitance model.

Figure 4.1 presents the surface admittance of the simulation results. Generally, the simulation results fit the admittance model. However, it is obvious that some noise was introduced, leading to the zigzag shape in the admittance of the simulation results. An

assumption is made that the noise may come form the reflection wave componet of Mur's ABC on the other side of the tube, since first-order Mur's ABC is not a perfectly absorptive boundary. Another assumption is that this noise may be caused the nature of the finite differential approximation. Discretization serves as a low-pass filter in this case. On the other hand, the simulation result fits the model not very well at high frequency. This is because the auxiliary functions $\psi_s^{(1)}$ and $\psi_s^{(2)}$ in Equation (2.26) are derived from the first-differential equations instead of the second-differential equations. This results in the less computational memory at the cost of accuracy.

CHAPTER 5
SUMMARY

We have presented and implemented ADE-FDTD for the broadband admittance model in an attempt to simulate the arbitrary boundary condition. Bayesian theorem was applied to the model selection and parameter estimation to fit the measured data. The finite differential differential approximation showed that the sound motion in the tube of which one side is terminated with the arbitrary material. This work shows that the broadband admittance model can be achieved numerically through ADE-FDTD, with parameters assigned from the Bayesian inference.

This work is limited to numerical verification and simulation results. Future work could include the validation work based on the real tube measurement and formulation of the admittance model of non-locally reacting model.

REFERENCES

[1] C.-H. Jeong, "Absorption and impedance boundary conditions for phased geometrical-acoustics methods," *J. Acoust. Soc. Amer.*, vol. 132, no. 4, pp. 2347–2358, Oct. 2012.

[2] F. Pind, A. P. Engsig-Karup, C.-H. Jeong, J. S. Hesthaven, M. S. Mejling, and J. Strømann-Andersen, "Time domain room acoustic simulations using the spectral element method," *J. Acoust. Soc. Amer.*, vol. 145, no. 6, pp. 3299–3310, Jun. 2019.

[3] C. K. Tam and L. Auriault, "Time-domain impedance boundary conditions for computational aeroacoustics," *AIAA J.*, vol. 34, no. 5, pp. 917–923, May 1996.

[4] K.-Y. Fung and H. Ju, "Broadband time-domain impedance models," *AIAA J.*, vol. 39, no. 8, pp. 1449–1454, Aug. 2001.

[5] Y. Reymen, M. Baelmans, and W. Desmet, "Efficient implementation of tam and auriault's time-domain impedance boundary condition," *AIAA J.*, vol. 46, no. 9, pp. 2368–2376, Sep. 2008.

[6] X. Li, X. Li, and C. K. Tam, "Improved multipole broadband time-domain impedance boundary condition," *AIAA J.*, vol. 50, no. 4, pp. 980–984, Apr. 2012.

[7] D. Dragna, P. Pineau, and P. Blanc-Benon, "A generalized recursive convolution method for time-domain propagation in porous media," *J. Acoust. Soc. Amer.*, vol. 138, no. 2, pp. 1030–1042, Aug. 2015.

[8] J. Zhao, M. Bao, X. Wang, H. Lee, and S. Sakamoto, "An equivalent fluid model based finite-difference time-domain algorithm for sound propagation in porous material with rigid frame," *J. Acoust. Soc. Amer.*, vol. 143, no. 1, pp. 130–138, Jan. 2018.

[9] J. Bin, M. Yousuff Hussaini, and S. Lee, "Broadband impedance boundary conditions for the simulation of sound propagation in the time domain," *J. Acoust. Soc. Amer.*, vol. 125, no. 2, pp. 664–675, Feb. 2009.

[10] R. Troian, D. Dragna, C. Bailly, and M.-A. Galland, "Broadband liner impedance eduction for multimodal acoustic propagation in the presence of a mean flow," *J. Sound Vibration*, vol. 392, pp. 200–216, Mar. 2017.

[11] A. Taflove, S. C. Hagness, W. Gwarek, M. Fujii, and S.-H. Chang, "Dispersive, Nonlinear and Gain Material," in *Computational Electrodynamics*, 3rd ed., A. Taflove and S. C. Hagness, Eds. Norwood, MA, USA: Artech house, 2005, ch. 9, pp. 353–406.

[12] K. Yee, "Numerical solution of initial boundary value problems involving Maxwell's equations in isotropic media," *IEEE Trans. Antennas Propag.*, vol. 14, no. 3, pp. 302–307, May 1966.

[13] N. Xiang and J. Blauert, *Acoustics for Engineers: Troy Lectures*, 3rd ed. New York, NY, USA: Springer Sci. & Business Media, 2021.

[14] T. Cox and P. d'Antonio, *Acoustic Absorbers and Diffusers: Theory, Design and Application*, 3rd ed. Boca Raton, FL, USA: CRC Press, 2017.

[15] J. B. Schneider, C. L. Wagner, and S. L. Broschat, "Implementation of transparent sources embedded in acoustic finite-difference time-domain grids," *J. Acoust. Soc. Amer.*, vol. 103, no. 1, pp. 136–142, Jan. 1998.

[16] J. Sheaffer, M. van Walstijn, and B. Fazenda, "Physical and numerical constraints in source modeling for finite difference simulation of room acoustics," *J. Acoust. Soc. Amer.*, vol. 135, no. 1, pp. 251–261, Jan. 2014.

[17] A. P. Zhao and A. V. Raisanen, "Application of a simple and efficient source excitation technique to the FDTD analysis of waveguide and microstrip circuits," *IEEE Trans. Microw. Theory Techn.*, vol. 44, no. 9, pp. 1535–1539, Sep. 1996.

[18] S. D. Gedney, "Introduction to the finite-difference time-domain (FDTD) method for electromagnetics," *Synthesis Lectures Comput. Electromagn.*, vol. 6, no. 1, pp. 1–250, Jan. 2011.

[19] J.-P. Bérenger, "A historical review of the absorbing boundary conditions for electromagnetics," *Forum Electromagn. Res. Methods Appl. Technol.*, vol. 9, no. 6, pp. 1–28, Jun. 2015.

[20] N. Xiang and C. Landschoot, "Bayesian inference for acoustic direction of arrival analysis using spherical harmonics," *Entropy*, vol. 21, no. 6, p. 579, Jun. 2019.

[21] N. Xiang, "Model-based bayesian analysis in acoustics—a tutorial," *J. Acoust. Soc. Amer.*, vol. 148, no. 2, pp. 1101–1120, Aug. 2020.

[22] K. H. Knuth, M. Habeck, N. K. Malakar, A. M. Mubeen, and B. Placek, "Bayesian evidence and model selection," *Digit. Signal Process.*, vol. 47, pp. 50–67, Dec. 2015.

[23] R. E. Kass and A. E. Raftery, "Bayes factors," *J. Amer. Statist. Assoc.*, vol. 90, no. 430, pp. 773–795, Jun. 1995.

[24] J. Skilling, "Nested sampling," in *AIP Conf. Proc.*, vol. 735, no. 1, 2004, pp. 395–405.